Applied Materials Today 24 (2021) 101159

Contents lists available at ScienceDirect

Applied Materials Today

journal homepage: www.elsevier.com/locate/apmt

Multifunctional approach to improve water oxidation performance with MOF-based photoelectrodes

Niloufar Afzali[a], Reza Keshavarzi[a,*], Shahram Tangestaninejad[a,*], Sixto Gimenez[b,*], Valiollah Mirkhani[a], Majid Moghadam[a], Iraj Mohammadpoor-Baltork[a]

[a] Department of Chemistry, Catalysis Division, University of Isfahan, Isfahan 81746-73441, Iran
[b] Insitute of Advanced Materials (INAM), University Jaume I, 12006 Castello de la Plana, Spain

ARTICLE INFO

Article history:
Received 27 May 2021
Revised 8 August 2021
Accepted 15 August 2021

Keywords:
MOF
Co-catalyst
Water oxidation reaction
Visible-light-responsive photocatalyst

ABSTRACT

Metal-Organic Frameworks (MOFs) are a group of compounds with high porosity and diverse capabilities in photoelectrochemistry. The use of these compounds as photocatalysts and photoelectrodes is still a strong challenge due to bulk and surface recombination issues. To solve this problem, we applied a dual strategy to simultaneously enhance charge separation and catalytic activity in MIL-125-NH_2 and UIO-66-NH_2 MOF photocatalysts. Mesoporous TiO_2 was used as electron-selective contact on the MOF surface (MOF/TiO_2) to minimize bulk recombination. On the other hand, to increase the MOF catalytic activity for water oxidation, a well-matched $Co_3(PO_4)_2$ (CoPi) co-catalyst (CoPi/MOF/TiO_2) was used. The obtained results showed that CoPi and TiO_2 were introduced in the MOF structure. The (CoPi/MOF/TiO_2) photoelectrodes showed a photocurrent density 26 times higher compared to the reference MOF at 1.23 V vs. RHE for PEC water oxidation of artificial seawater, validating the developed strategy for further photocatalytic and photoelectrochemical applications.

1. Introduction

Photo-electrochemical water splitting with sunlight to produce H_2 stands out as a promising and cost-effective technology to provide sustainable energy vectors and feedstocks for the chemical industry.[1] In photoelectrochemical water splitting, the two half-reactions involved are hydrogen evolution and oxygen evolution occurring at the cathode, (HER) H^+/H_2 (0 V vs. RHE) and anode, (OER) O_2/H_2O (1.23 V vs. RHE), respectively.[2, 3] The main challenges of this process relate to the slow kinetics of OER, where four holes must be injected into the solution to produce one oxygen molecule.[4, 5] For this reason, increasing the efficiency of the OER reaction is mandatory to obtain more competitive photoanodes.

Fujishima and Honda were the first researchers reporting the ability of TiO_2 to generate O_2 under UV irradiation, which is around 4% of the total solar spectrum. The development of effective water oxidation catalysts (WOCs) from low-cost, earth-abundant elements and high-performance to operate under visible light (almost half of the incoming solar energy) is one of the main challenges in the field of solar energy conversion. [5, 6] Recently, metal organic frameworks (MOFs) like MIL-125 and UiO-66 have demonstrated to be promising candidates to split water under solar irradiation, since both sensitizer and catalytic center can be integrated in a single structure and produce O_2 as a result of photoelectrochemical reaction with water.[7, 8] MOFs are a bunch of 1, 2 or 3-dimensional structures composed of metal nodes and organic linkers. These structures feature key advantages such as high crystallinity, surface area, porosity, thermal and chemical stability, and tunability to design them by changing the linkers or nods. These interesting properties allow the application of these frameworks in a plethora of applications including: selective drug delivery,[9] CO_2 capture,[10] hydrogen storage,[11] catalysis,[12] organic synthesis,[13] degradation of pollutants,[14] photoelectrochemical,[15] and photocatalytic[16] water splitting. MIL-125-NH_2 and UIO-66-NH_2 with appropriate band gap (2.6 eV) are some of the successful MOFs that were used as photocatalysts in OER under visible light irradiation.[17, 18] In spite of all these advantages, MOFs have two important drawbacks to operate as photocatalysts, which limit their applicability: excessive electron-hole recombination,[19] and poor catalytic activity, which lead to large overpotentials.

* Corresponding authors.
E-mail addresses: R.Keshavarzi@chem.ui.ac.ir, R.keshavarzi85@gmail.com (R. Keshavarzi), stanges@sci.ui.ac.ir (S. Tangestaninejad), sjulia@fca.uji.es (S. Gimenez).

https://doi.org/10.1016/j.apmt.2021.101159

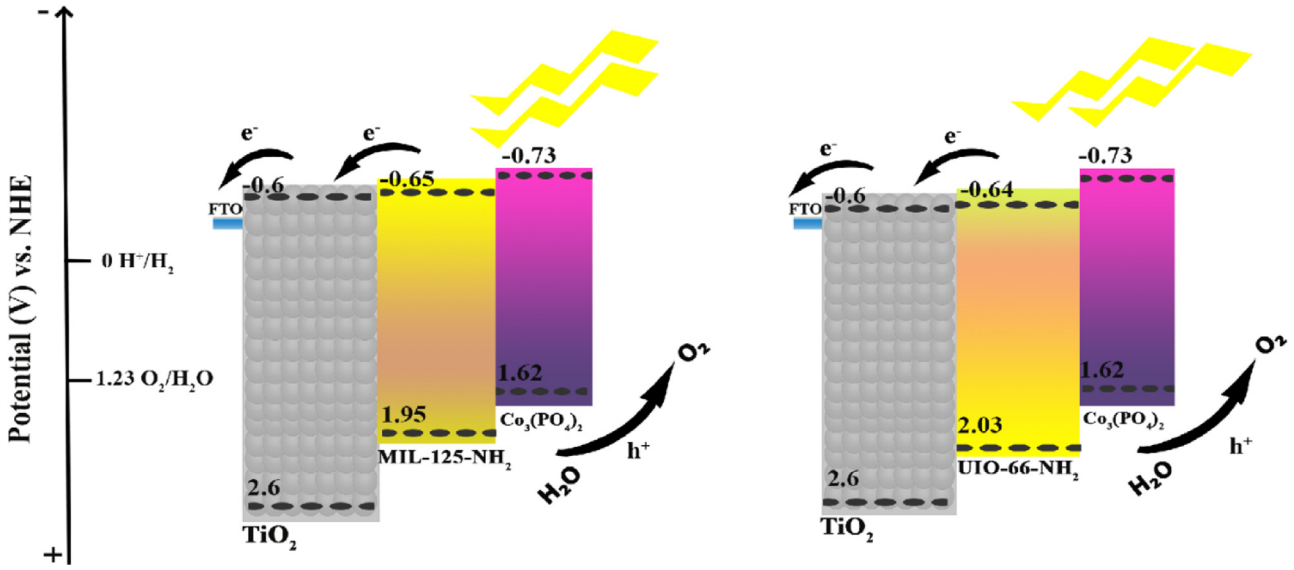

Scheme 1. Estimated band diagram of the a) CoPi/ MNH /TiO_2, and b) CoPi/ UNH /TiO_2 for water oxidation.[19, 28-30]

Among the different strategies to minimize recombination, the introduction of a blocking layer to the MOF/FTO interface (FTO as a charge collection substrate) is considered one of the most promising approaches. Recent reports showed that TiO_2, ZnO, and SnO_2 are suitable candidates as blocking layer.[20] Also, the coupling of MOFs with co-catalysts like IrO_2 and RuO_2 can overcome the poor photocatalytic activity of MOFs towards OER.[21-23] Rare earth metal oxides of IrO_2 and RuO_2 operate under acidic conditions. Thus, it will be very important to develop earth-abundant alternatives under neutral pH conditions, which are more environmentally friendly, and potentially with less corrosion problems. Co-based catalysts such as CoPi have been considered as promising alternatives to noble metal-based counterparts for driving OER, due to their abundance, environmental friendliness, high catalytic activity, good stability, low cost and operation under neutral conditions.[24-27]

In this study, we show the dramatic improvement on OER activity for two different MOFs, by integrating both strategies. The MIL-125-NH_2 and UIO-66-NH_2 with 2-aminoterephthalic acid linkers (where the HOMO position is located), and the metal oxide clusters (where the LUMO position is located) created metal organic frameworks featuring an adequate band gap for efficient visible light harvesting. To minimize charge recombination, anatase TiO_2, which has tunable conductivity and adequate band position relative to MIL-125-NH_2 and UIO-66-NH_2, was used to effectively prevent the back recombination of collected electrons on the FTO substrate with photogenerated holes within the MOFs. To improve the water oxidation activity of both MIL-125-NH_2 and UIO-66-NH_2, $Co_3(PO_4)_2$, (CoPi) which is an earth-abundant co-catalyst and compatible with the HOMO position of these MOFs, was used. The estimated band diagrams of the heterostructured photoelectrodes are shown as **Scheme 1**. To the best of our knowledge, simultaneous implementation of these strategies for high efficiency water splitting with MOFs has not been reported so far. The obtained results showed the promising performance of this new MOFs design.

2. Experimental method

2.1. Synthesis of mesoporous TiO_2 solution

In order to synthesize mesoporous TiO_2 solution, block copolymer Pluronic P123 (Sigma-Aldrich, 1.0 g) was dissolved in 1-butanol (9.07, Aldrich) by stirring. Individually, on a different baker, HCl (2.42 g, Merck, 36 wt%) was added to tetraethyl orthotitanate (3.17 g, Sigma-Aldrich) under vigorous stirring. After thirty minutes of stirring, the copolymer solution was added to the HCl/$Ti(OEt)_4$ solution and then, the solution was subjected to continuous and intense stirring for three hours to prepare a clear TiO_2 solution.[20]

2.2. Synthesis of UiO-66

The UiO-66 was synthesized based on the procedure reported by Cavka et. al. [31] In a typical procedure, terephthalic acid (123 mg, 0.75 mmol) as a linker was dissolved in N,N‘- dimethylformamide (7.5 ml). On the other hand, $ZrCl_4$ (125 mg, 0.54 mmol) was also dissolved in DMF (7.5 ml). The $ZrCl_4$ solution was added to the terephthalic solution gently and stirred to obtain a uniform solution. The resulting mixture was placed in a Teflon-lined stainless-steel autoclave for 24 hours at 120 °C. The solid white powder was separated with the appropriate sinter disc, stirred with methanol overnight at 70°C and dried in a vacuum oven at 120 °C.

2.3. Synthesis of MIL-125

Titanium(IV) isopropoxide (0.3 mL) and BDC (250 mg) were added to a mixture of methanol (0.5 mL) and DMF (4.5 mL) and stirred at room temperature until a homogeneous solution was obtained. Then, the mixed solution was placed in a Teflon-lined stainless-steel autoclave and heated at 80 °C for 48 h. The reaction was cooled down to room temperature and the obtained precipitate was collected by filtration. The white precipitate was washed three times with DMF to remove the remaining unreacted titanium isopropoxide from the porous framework. The resulting solid was rinsed several times with methanol and dried at 80 °C under vacuum for 5 h.[32]

2.4. Synthesis of MIL-125-NH_2 (MNH)

A solvothermal synthesis was used to prepare MIL-125-NH_2.[33] 2-aminoterephthalic acid (0.95 g, 5.26 mmol, 99%, Aldrich) was dissolved in DMF (13.3 mL, 99.9%, Aldrich). Then, $Ti(O^iPr)_4$ (0.95 mL, 3.23 mmol, 99 %, Aldrich) was introduced drop by drop to the mixture. Afterwards, the mixture was placed in a Teflon-lined

stainless steel autoclave, which was heated at 110 °C for 72 h. Finally, MIL-125NH_2 was washed with DMF to remove of organic linker and then with methanol to exchange the solvent. Activation of MOF was made by drying at 200°C for 5h.

2.5. Synthesis of UIO-66-NH_2 (UNH)

UiO-66-NH_2 was synthesized by hydrothermal method via adding zirconium chloride (7 mmol) to 2-amino terephthalic acid (ATA). The solution was stirred in DMF (40 mL) for 30 min. Then, the suspension was heated for 24 h at 120 °C. Afterwards, the sample was recovered by centrifugation and rinsed several times with methanol to extract the remaining unreacted metal salts/organic species. For activation, the solid was kept in DMF and methanol for 72 h and was separated by centrifugation. MOF was activated by heating at 200°C for 5h.[29]

2.6. Synthesis of CoPi /MNH and CoPi /UNH nanocomposite

The synthesis of the CoPi nanoparticles was carried out according to a reported procedure.[34] To synthesize CoPi/MNH or CoPi/UNH nanocomposite, Cobalt(II) chloride hexahydrate (0. 2 mol, Sigma-Aldrich) and CTAB (0.04 mol) was dissolved in water (10 mL) and then, 6ml of NaOH (2molar, Sigma-Aldrich) was added to the solution. Then, 500 mg of activated MNH or UNH was added to the mixture and kept under stirring during 72 h at room temperature. Ethanol (20 ml or 30 ml, Merck, 99.9%), was added into CoPi /MNH or CoPi /UNH to wash this nanocomposite twice, and the final solutions were centrifuged at 4500 rpm for 10 min to obtain nanoparticles. This nanocomposite was activated at 200°C for 5 h, twice.

2.7. Fabrication of MIL-125 and UIO-66 nanocomposite on FTO substrate

MIL-125 and UIO-66 nanocomposites were coated on FTO glasses (solaronix, ~ 7 Ω/sq) by doctor blade method from suspensions of MIL-125 and UIO-66 in water and acetylacetonate (50 mg of MOF, 1000 µL H_2O and 50 µL of acetylacetonate), sonicated for 1 h. The coated layers were stabilized at 170 °C for 1 h (heating rate: 5 °C/min). These prepared films were named MIL-125 and UIO-66

2.8. Fabrication of mesoporous TiO_2 film

A dip coating system (Advanced Equipment Engineering Company, Iran) with a withdrawal rate of 30 mm/min was used to deposit the mesoporous TiO_2 film on a Fluorine-doped tin oxide (FTO) conducting glass (solaronix, ~7Ω/sq). The relative humidity was set at 25% - 30% at 25 °C in an electronic dip-coating chamber. The layer was deposited by directly transferring the deposited layer on a hot plate for 15 min at 300 °C. The films were annealed under air at 450 °C for 1 h (heating rate: 1 °C/min) for removing the block copolymers as structure-directing agents. [20]

2.9. Fabrication of CoPi /MNH and CoPi /UNH nanocomposite on mesoporous TiO_2 film

FTO (solaronix, ~ 7 Ω/sq) coated by mesoporous TiO_2, was covered with CoPi /MNH nanocomposite by doctor blade method from the suspension of CoPi/MNH in water and acetylacetonate (50 mg of MOF, 1000 µL H_2O and 50 µL of acetylacetonate) sonicated for 1 h. This suspension was then deposited onto FTO/TiO_2 and fixed at 170 °C for 1 h (heating rate: 5 °C/min). This prepared sample is named CoPi/MNH/TiO_2 nanocomposite. We used the same method to fabricate MNH on mesoporous TiO_2 (MNH/TiO_2) without using MIL-125-NH_2. CoPi /MNH was also coated on FTO without the TiO_2 layer to obtain CoPi /MNH electrode. This method was also used to fabricate the CoPi on FTO without the layer of mesoporous TiO_2 and named CoPi electrode. We used the same procedure to prepare UIO samples by replacing MIL-125-NH_2 with UIO-66-NH_2 for CoPi/UNH/TiO_2, CoPi /UNH, UNH/TiO_2 electrodes.

2.10. Optical and photoelectrochemical characterization

UV-vis absorption spectra were carried out on solid samples using a JASCO V-670 spectrophotometer. To determine the surface area, pore volume, and pore size distribution of the MOFs, BELSORP mini II instrument according to adsorption-desorption of N_2 gas at 350 °C was applied. Particle size was determined by high-resolution transmission electron microscope (HRTEM, FEI Tecnai G20) with an accelerating voltage of 200 kV. ICP analysis was carried out with a Perkin-Elmer Optima 7300 DV spectrometer to determine the amount of co-catalyst. Powder X-ray diffraction (XRD) analyses were performed on a D8 Advanced Bruker instrument utilizing Cu $K\alpha$ radiation (λ = 1.5406 Å). Energy dispersive X-ray analysis (EDX) and field emission scanning electron microscopy (FE-SEM, S4160 Hitachi Japan) was used to study the MOF texture and the thickness of the deposited films.

PEC measurements were carried out using an IM6x electrochemical station (Zahner, Germany). A solar simulator (Sharif) was used to illuminate the photoelectrodes at 1 sun (AM1.5G, 100 mW/cm^2) illumination. Electrochemical impedance spectroscopy (EIS) was carried out in the dark, at an applied potential of 0.6 V (vs. Ag/AgCl/saturated KCl, equal to 1.23 V vs. RHE), with a 10 mV AC amplitude and a frequency range of 10^{-2} Hz to 10^5 Hz. Transient photocurrent densities were obtained by chopped illumination (1 sun) under application of a constant potential of 1.23 V vs. RHE. In order to investigate the activity of the working electrode, we used a three-electrode configuration using CoPi /MNH /TiO_2 films of 1 cm^2 size on FTO as the working electrode (WE), Pt mesh as counter electrode (CE) and a Ag/AgCl electrode as reference electrode (RE) in artificial seawater electrolyte solution: 0.029 mol L^{-1} Na_2SO_4, 0.055 mol L^{-1} $MgCl_2$ and 0.42 mol L^{-1} NaCl. [35] To compare between CoPi /MNH /TiO_2, MIL-125-NH_2/TiO_2 and CoPi /MNH, and also UIO samples, the same method was used. In the Pyrex photoelectrochemical cell containing the three electrodes, N_2 gas was bubbled to remove dissolved O_2, after this, the light was switched on under stirring at room temperature. The charge-injection efficiency η_{CI} and charge-separation efficiency η_{CS} were calculated by the following equations:

$$\eta_{CI} = j_{H2O}/j_{hs} \quad (1)$$

$$\eta_{CS} = j_{hs}/j_{abs} \quad (2)$$

Where $_{jH2O}$ is the photocurrent density in water, j_{hs} is the photocurrent density in the presence of a hole scavenger, and j_{abs} is the maximum absorbed photocurrent that can be obtained from:

$$j_{abs} = e/hc \int I_\lambda \left(1 - 10^{-A}\right) d_\lambda . \quad (3)$$

where I_λ is the light intensity at a certain wavelength λ, and A is the absorption coefficient, e the elemental charge, h the Planck constant, and c the speed of light.[36]

3. Results and discussion

The CoPi/MNH/TiO_2, MNH/TiO_2, and CoPi/MNH materials and also the same UIO-66-NH_2 (UNH) based photocatalysts were characterized using Powder XRD (PXRD) (Fig. 1a and b) after scratching the samples from the glass substrates. The recorded PXRD patterns of MOF samples evidence the tetragonal structure of MIL-125-NH_2 (group I 4/m m m) and the cubic structure of UIO-66-NH_2 (group F

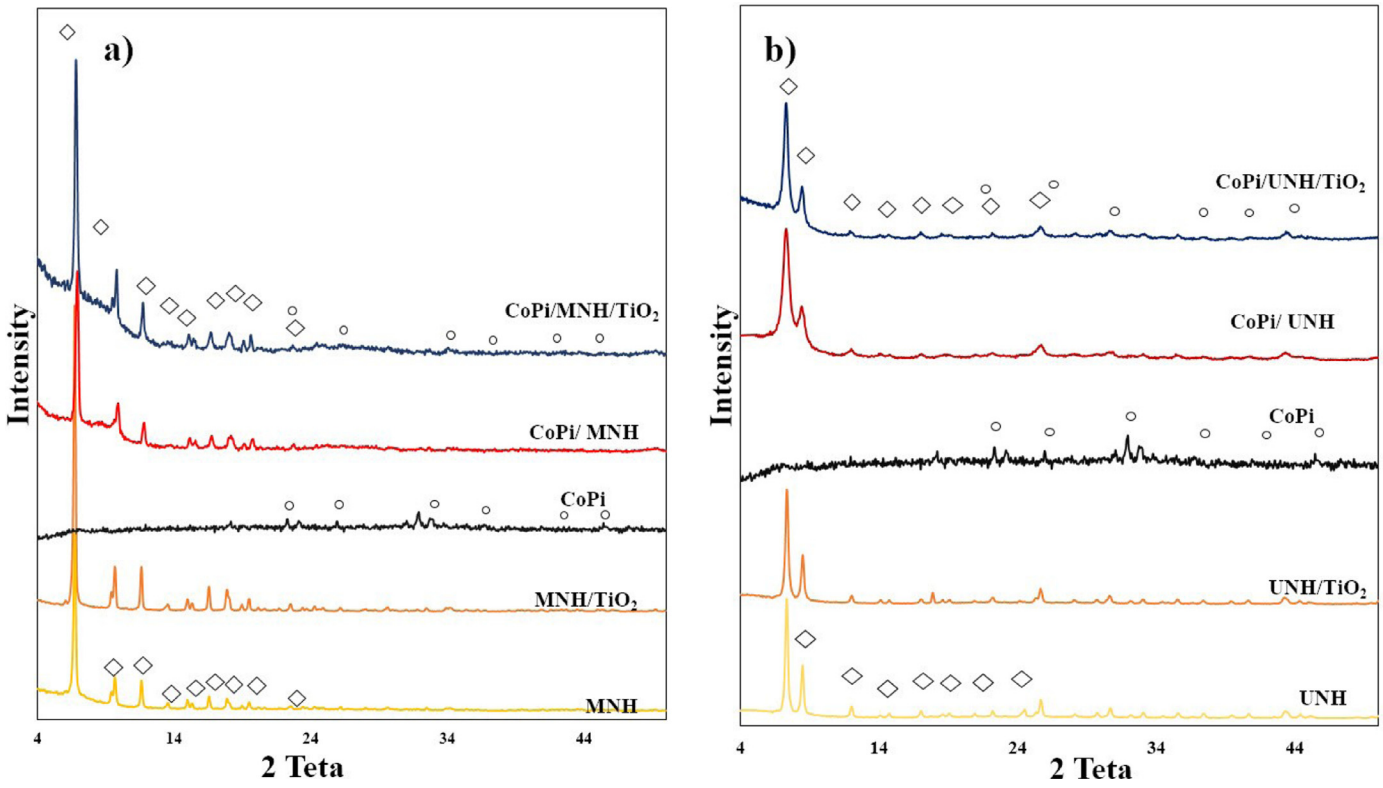

Fig. 1. Powder XRD patterns of a) MNH, MNH/TiO_2, CoPi, CoPi/ MNH and CoPi/ MNH /TiO_2 and b) UNH, UNH/TiO_2, CoPi, CoPi/UNH and CoPi/UNH/TiO_2 materials. The symbols of (◊) and (○) in Fig.1a show diffraction peaks for MNH and CoPi, respectively. Moreover, the symbols of (◊) and (○) in Fig.1b show diffraction peaks for UNH and CoPi, respectively.

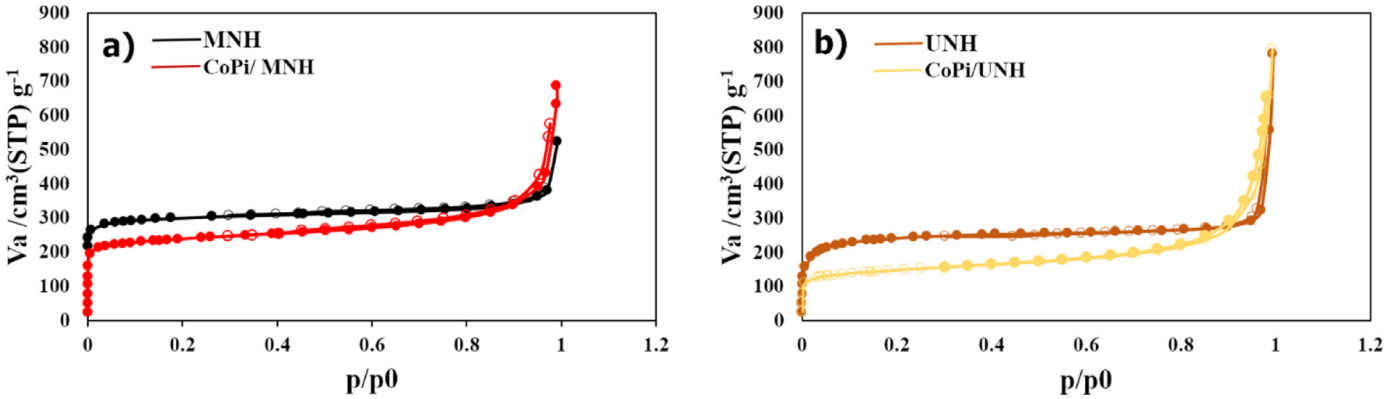

Fig. 2. BET surface area analysis: Adsorption-desorption isotherms of the a) MNH and b) UNH based photocatalysts.

m -3 m). In all cases, the MOF structure was not altered after synthesis of CoPi/MOF/TiO_2, MOF/TiO_2 and CoPi/MOF.[37, 38] On the other hand, the low volume fraction of CoPi explains the absence of the related diffraction peaks (see Supplementary Material for a more detailed justification). Additionally, the results show that after synthesis of CoPi in the presence of MOFs, the crystallinity of pristine MOFs was maintained. The relatively low thickness of the TiO_2 layer (260 nm) (Supplementary Material, Fig. S1) also explains the absence of any diffraction peaks for mesoporous TiO_2.[39] UIO-66 and MIL-125 without NH2 groups were also synthesized to investigate catalytic activity in the dark and under illumination. The related XRD patterns were shown in Supplementary Material, Fig S2).

N_2 adsorption-desorption isotherms on UiO-66, MIL-125 (Fig. S3) and UNH, CoPi/ UNH, MNH, CoPi/ MNH (Fig. 2) showed an overall type I isotherm behavior for all four samples, as expected for microporous materials.[33] The S_{BET} for UNH, CoPi/UNH, MNH, CoPi/MNH was 934.72, 552.77, 1183.6, and 908.1 m^2 g^{-1}, respectively. These results are in good agreement with the presence of CoPi in the MOF composite. Also, the S_{BET} for UiO-66, MIL-125 was 1100 and 1380 m^2 $g^{-}1$, respectively. The pore size distributions insulated from the micropores range (MP) are shown as Supplementary Material, Fig. S4. The size of the micropores decreases as a result of CoPi incorporation and consequently CoPi/UNH and CoPi/MNH possessed the lowest micropore size. This is probably due to the partial occupation of some pores by CoPi.[40]

FE-SEM characterization of UNH, CoPi/UNH, MNH, CoPi/MNH (Fig. 3a, b, d, and e) show octahedral cubic morphology for UNH and CoPi/UNH samples with average size of 90-120 nm, and truncated bipyramids with an average size of about 350 nm for MNH and CoPi/MNH in good agreement with previous reports. [33, 41, 42] The samples containing CoPi, reveal CoPi agglomerates with

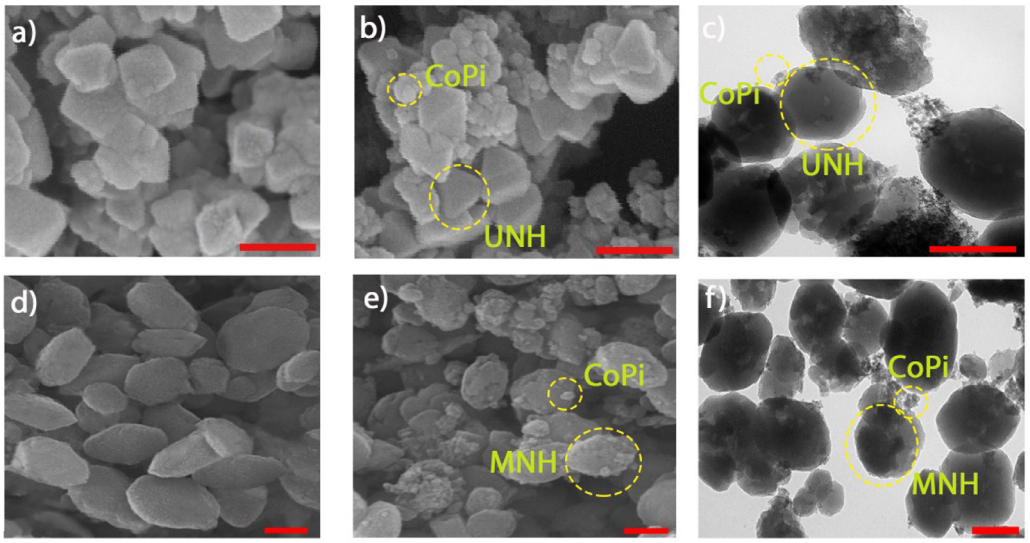

Fig. 3. FE-SEM images of a) UNH, b) CoPi/UNH. d) MNH, e) CoPi/MNH. TEM images of c) CoPi/UNH, and f) CoPi/MNH (Scale bar 200 nm in all micrographs).

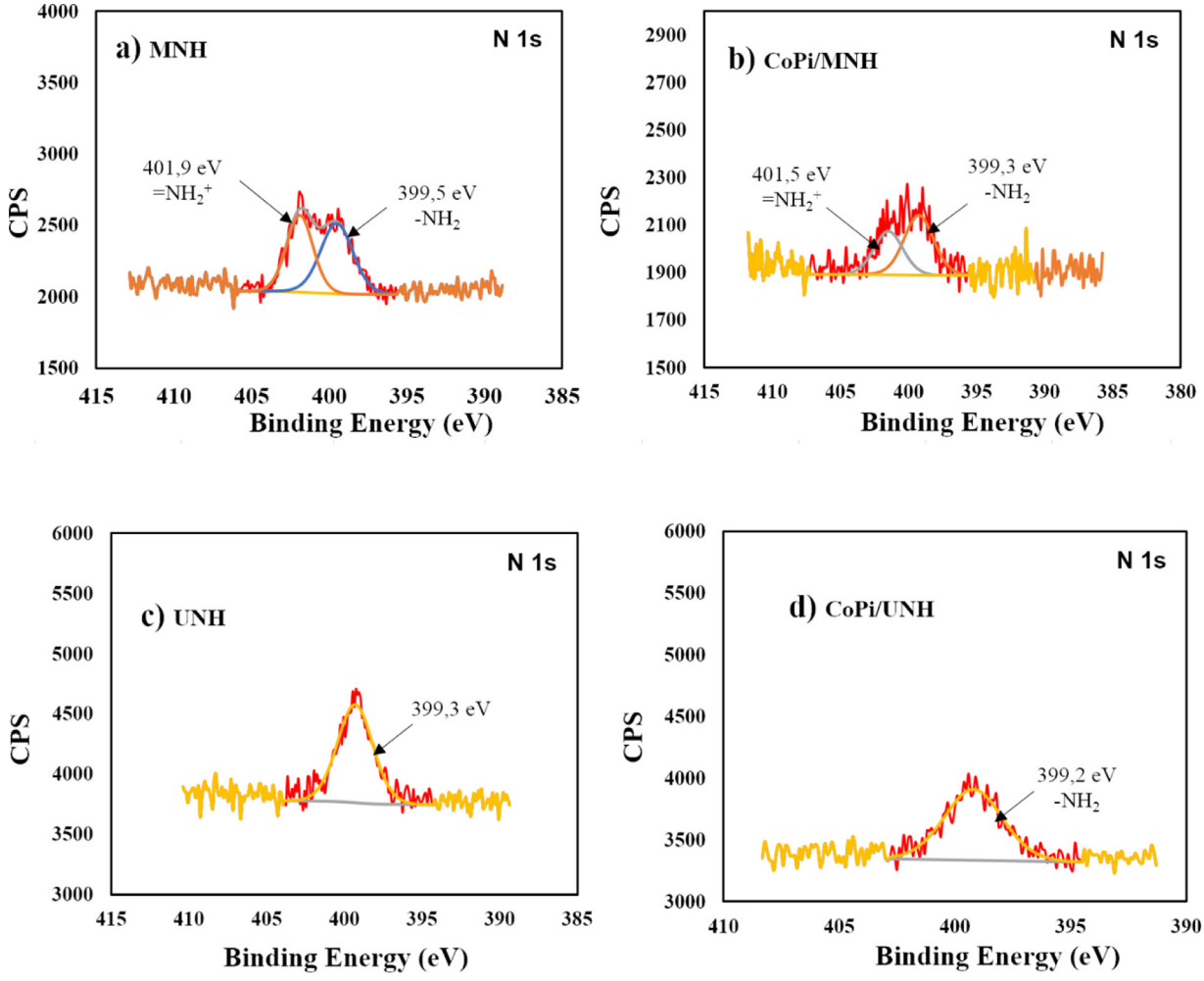

Fig. 4. High-resolution XPS spectra of a) N 1s for MNH, b) and CoPi/ MNH, and c) N 1s for UNH, and d) CoPi/ UNH.

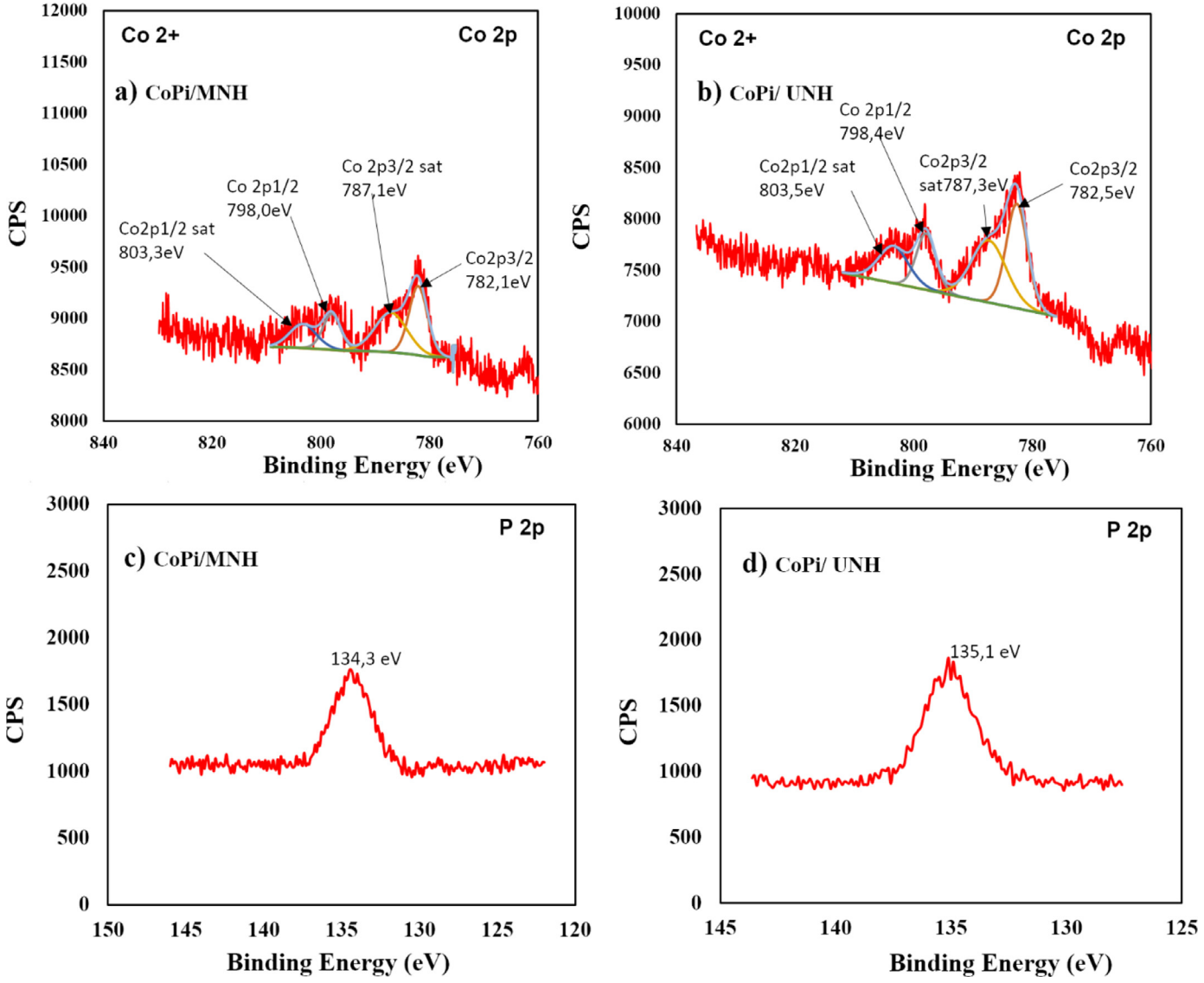

Fig. 5. High-resolution XPS spectra of (a and b) Co 2p, and (c and d) P 2p for CoPi/ MNH, and CoPi/ UNH, respectively.

sizes ranging from 10 to 40 nm on the surface of the MOFs. Cross-section images of CoPi/ MNH /TiO_2, and CoPi/UNH/TiO_2 (Supplementary Material, Fig S1) reveal that the thickness of the coated TiO_2 was around 260 nm and the thickness of CoPi/MOFs for CoPi/MNH/TiO_2 and CoPi/UNH/TiO_2 was 560 nm and 580 nm, respectively. Similar Co content (about 7%) was quantified through Energy Dispersive X-ray spectroscopy (EDX) on these samples, (Supplementary Material, Table S1). Furthermore, elemental mapping for CoPi/MNH and CoPi/UNH (Supplementary Material, Fig S5a and b) clearly shows that CoPi is homogeneously decorated on the MIL-125-NH_2 and UIO-66-NH_2 samples. ICP-OES analysis on CoPi/ MNH and CoPi/ UNH revealed 6.5 and 7.8 wt-% Co, respectively, in line with EDX results. Tiny nanoparticles of CoPi with 10-40 nm diameter were identified by TEM on the surface of the MOF materials (Figs 3c and f).

XPS analysis was performed to confirm the presence of cobalt and the electronic interactions between MOFs in the photocatalysts. Supplementary Material, Fig S6 (a-b) show the XPS survey spectrum for MNH and CoPi/MNH (S6 a), and UNH and CoPi/UNH (S6 b).

The high-resolution N 1s spectrum was monitored to obtain further information about the interaction between MOFs and CoPi. The two bands at 399.5 and 401.9 eV matching with the N of $-NH_2$ stretching group in MNH are shown in fig 4a and b, while the band at 399.2 eV attributed to $-NH_2$ group in UNH is shown in fig 4c and d. There are no differences between these groups in MNH, and CoPi/MNH and also in UNH, and CoPi/UNH. This clearly indicates that there is no electronic interaction between CoPi, and $-NH_2$ group of MOFs $-NH_2$ linkers.[29, 43] The typical peaks located at about 782 and 787 eV in the Co 2p3/2 region, show that cobalt is present in the Co^{2+} state (Fig 5a and b). Also, two shake-up satellites and two spin–orbit doublets in the Co 2p spectrum were observed (the peaks around 787 eV in Co 2p3/2 and 803 eV in Co 2p1/2 are assigned to Co^{2+}, and the peaks around 782 eV in Co 2p3/2 and 798 eV in Co 2p1/2 are ascribed to Co^{3+}).[44] On the other hand, the binding energy of P 2p was about 135.4 eV, (Fig 5c and d) which is characteristic of P in the form of PO_4^{3-} in phosphate group of CoPi co-catalysts.[30]

Supplementary Material, Fig S5a shows the UV-visible absorbance (A) spectra of the different samples. The maximum theoretical photocurrent could be extracted after integration of the calculated absorptance ($a = 1 - 10^{-A}$), as showed in Supplementary Material, Fig S7. Furthermore, the bandgaps of UNH/TiO_2, UNH, MNH and MNH/TiO_2 were identified from Tauc plots for indirect

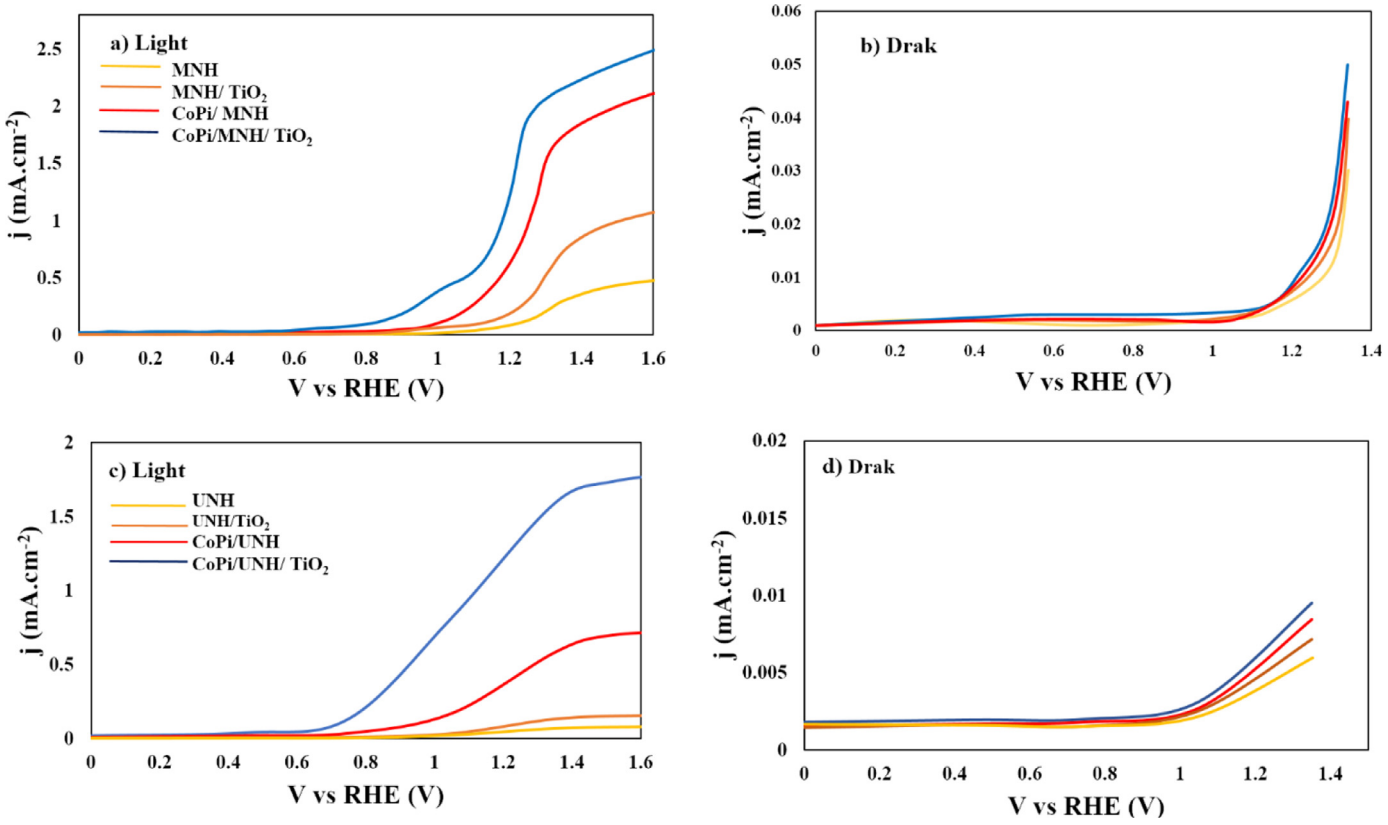

Fig. 6. Linear sweep photovoltammograms of MOF composites in artificial seawater electrolyte in the dark and under illumination at 100 mW•cm^{-2}.

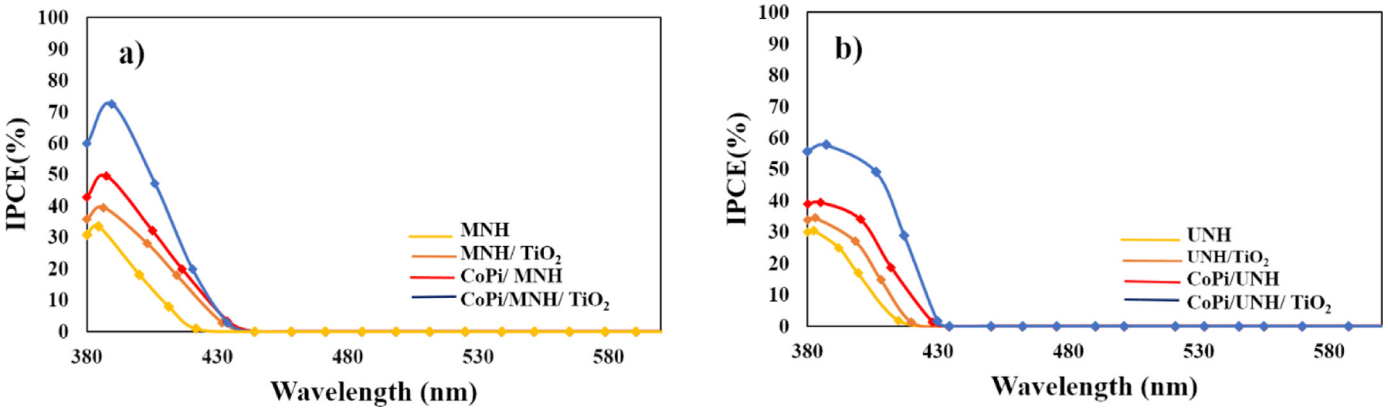

Fig. 7. Wavelength-dependent IPCE spectra of a) MNH and b) UNH based composites at 1.23 V vs RHE.

transitions, as shown in Supplementary Material, Fig S7 b and d. The obtained bandgaps are in good agreement with the energy diagrams showed in Scheme 1.[29, 33, 45]

Linear sweep voltammograms in artificial seawater were carried out in the dark and under illumination. The j-V curves did not show significant current density under illumination for both UIO-66 and MIL-125 samples (Supplementary Material, Fig S9). This agrees well with the large bandgap and the low optical absorption for MIL-125, as well as the low surface area and limited access to active sites for UIO-66.

At potentials below 1 V vs. RHE, dark current density was negligible (Fig. 6). Under visible light irradiation, the MOF, MOF/ TiO_2, CoPi/MOF, and CoPi/MOF/TiO_2 showed photocurrent densities up to 1.8 mA•cm^{-2} for the optimized heterojunctions. Concomitantly, the onset potentials for photocurrent can be ranked as MOF > MOF/TiO_2 > CoPi/MOF > CoPi/MOF/TiO_2. Simultaneously, under visible light illumination at 1.23 V vs. RHE, the current density was increased, accordingly. The photocurrent density is higher for MNH compared to UNH, probably due to the higher specific surface area of MNH, which facilitates charge transfer to the solution.[45] This is consistent with the calculated charge injection efficiency showed in Supplementary Material, Fig. S10. The photocurrent densities also increase with the presence CoPi, and TiO_2 compared to the reference materials. This can be attributed to the lower charge recombination and higher charge separation and injection efficiency in the presence of TiO_2 and CoPi co-catalyst. Chronoamperometric measurements with chopped illumination (Supplementary Material, Fig S11) are fully consistent with the results showed in Fig 6. Blank measurements on TiO_2 and TiO_2/CoPi samples did not show any meaningful current density (Supplementary Material, Fig S9).

IPCE measurements at 1.23 V vs RHE have been carried out and are included as Fig. 7. The main information relates to the

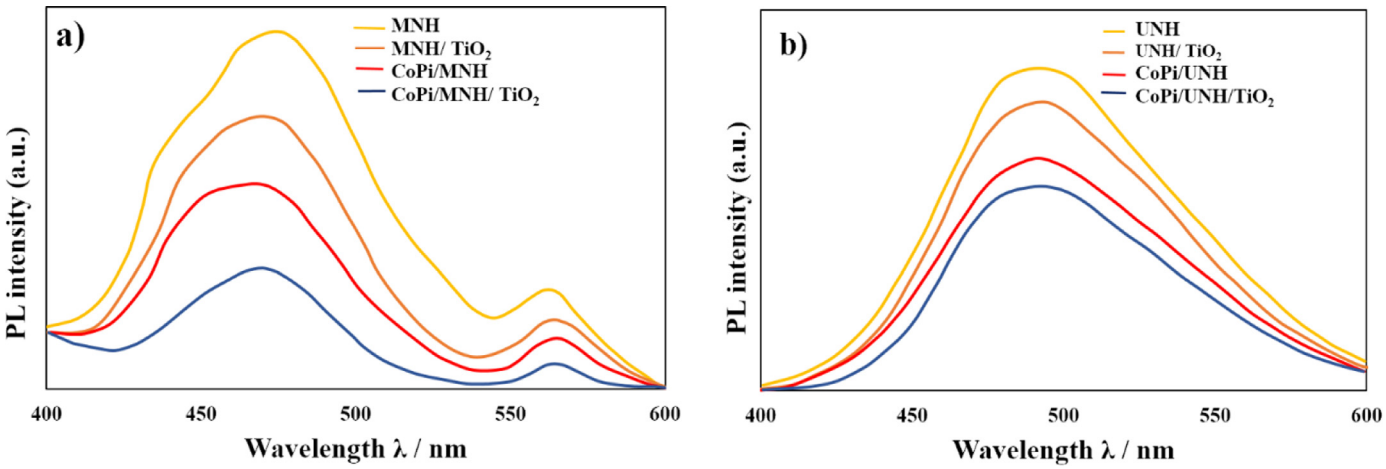

Fig. 8. Photoluminescence spectra (λ_{Ex} = 350 nm) of a) MNH, and b) UNH based nanocomposites.

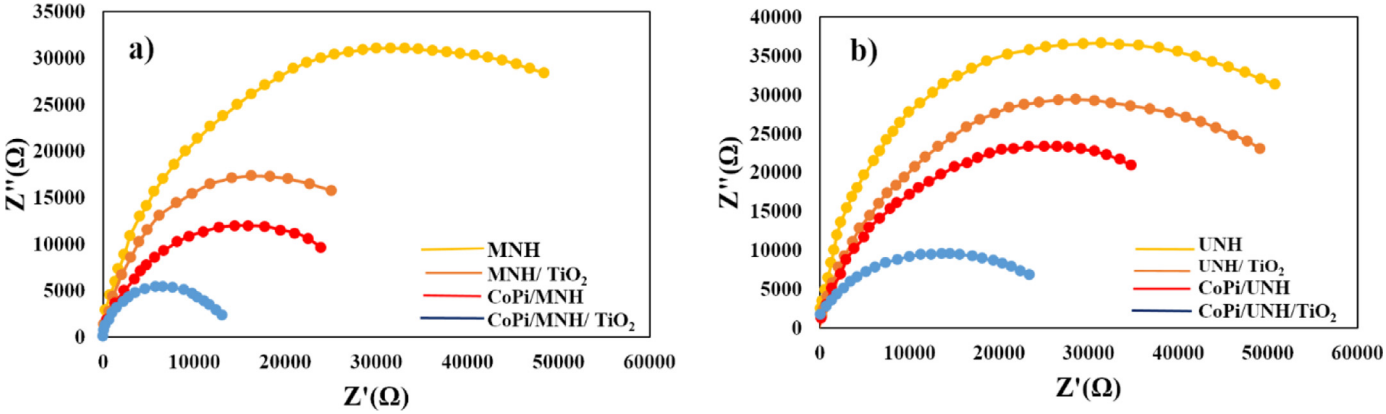

Fig. 9. Nyquist plots of a) MNH, and b) UNH based photoelectrodes obtained at 1.23 V vs RHE.

enhanced charge collection efficiency at the wavelengths < 450 nm. The optimized heterojunctions with both MOF photosensitizers (MNH and UNH), after introduction of the electron selective (TiO_2) and hole selective and catalytic (CoPi) layer exhibit wider spectral activity (photocurrent up to 430 nm) compared to the original MOF sensitizers, although the main improvement is related to the conversion efficiency at the peak wavelengths, which increases from around 30% to 60-70% in both materials, highlighting the enhanced charge injection efficiency after heterostructuring.

The highest photocurrent over CoPi/MOFs/TiO_2 demonstrate the enhanced lifetime and charge separation efficiency of the photogenerated charge carriers via the interaction among CoPi, MOFs and TiO_2. This is consistent with the photoluminescence (PL) measurements (Fig. 8) obtained over CoPi/MOFs/TiO_2, which is much weaker compared to MOF and MOFs/ TiO_2, and CoPi/MOFs.[46-49]

Further mechanistic information was obtained by impedance spectroscopy measurements. Nyquist plots obtained at 1.23 V vs RHE in the dark (Fig 9), systematically showed a single semicircle for all samples. The arc diameter (attributed to the charge-transfer resistance at the photoelectrode/electrolyte interface)[50, 51] was decreasing as the photoelectrode performance improves, consistently with the higher slope of the j-V curve (Fig 6).

Complementarily, charge-separation efficiency and the charge-injection efficiency were determined by additional photoelectrochemical characterization in the presence of a sacrificial hole scavenger (Na_2SO_3) by eqs 1–3 (dashed line in Supplementary Material, Fig S10 and S12). Fig S10 clearly illustrates that CoPi is responsible for a remarkable increase of the charge injection efficiency and confirms the improvement in PEC performance by enhancing this charge transfer step, either by the suppression of surface recombination or by promoting surface catalysis. On the other hand, the charge separation efficiencies of pure MOFs are enhanced by heterojunction with TiO_2 (see Supplementary Material, Fig. S12) reinforcing the hypothesis that TiO_2 provides an efficient electron selective contact responsible for increasing charge separation efficiency and subsequently photocurrent density. Enhanced charge separation efficiencies in CoPi/MOFs/TiO_2 are consistent with the decreased photoluminescence of MOFs in the presence of CoPi and TiO_2. As expected, the charge injection efficiency (Fig S10.) is significantly enhanced, after coupling MOFs with CoPi and TiO_2, reaching 71% by CoPi/MNH/ TiO_2 at 1.23 V vs RHE. The overall enhancement can be related to the fact that the photogenerated carriers undergo decreased bulk recombination (enhanced charge separation efficiency) with the incorporation of TiO_2 and accelerated surface catalysis (or suppressed surface recombination) with the incorporation of CoPi. Overall, the synergistic effect of the developed heterojunction and co-catalyst modification, CoPi /MOFs/TiO_2 photoelectrode heterostructures leads to promising water oxidation kinetics.

The stability of the CoPi/MOFs/TiO_2 was assessed by cronoamperometry at 1.23 V vs RHE for 5000 seconds, and the photocurrent density was approximately constant during this time (Fig 10 b and d). Interestingly, the photocurrent density decreased less than 10% during the recorded time, offering promising stability for further upscaling studies. Finally, a remarkable > 93 % Faradaic effi-

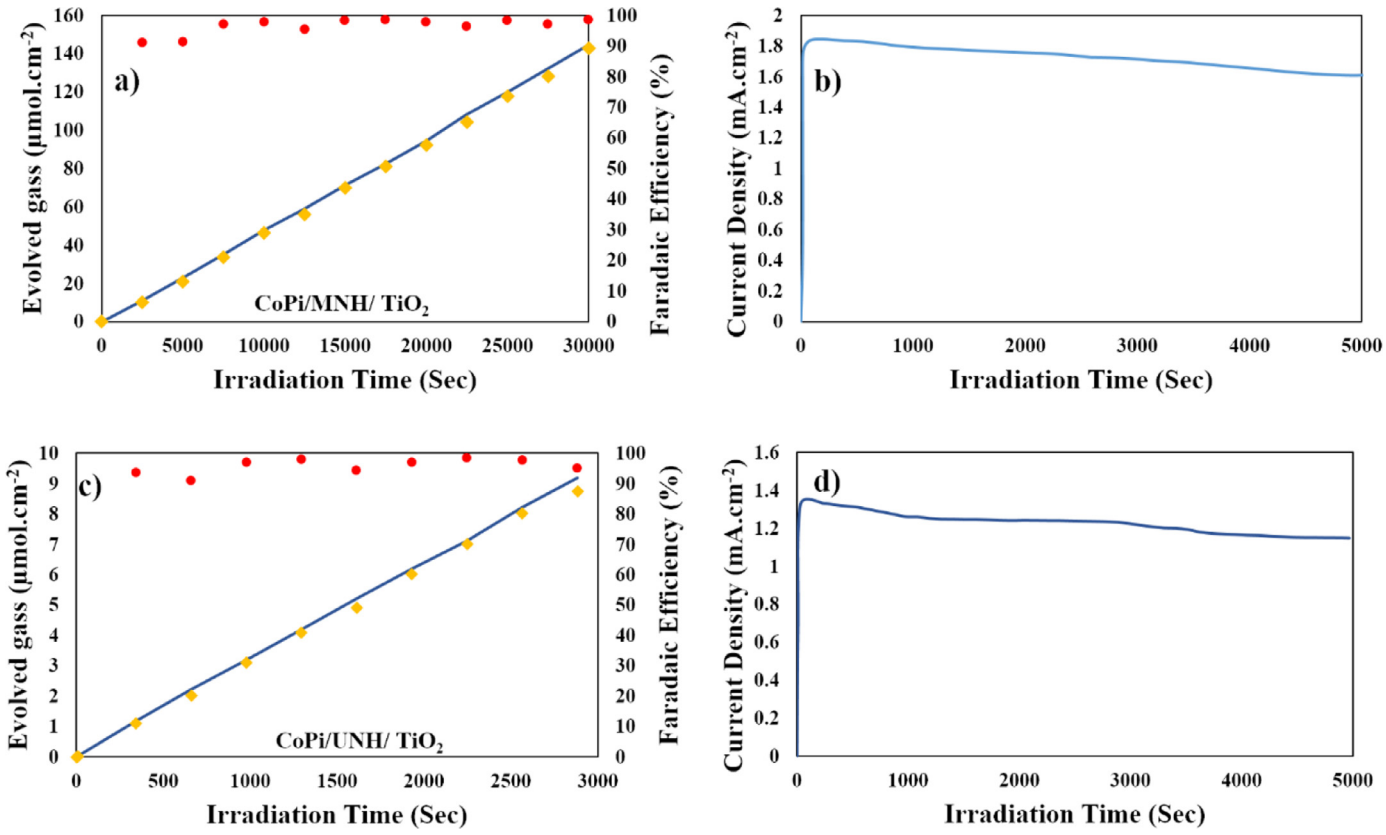

Fig 10. a and c) Theoretical (blue line) and measured (yellow square) O_2 evolution, along with Faradaic efficiency (red circles) and b and d) Chronoamperometric measurement of a CoPi/MOFs/ TiO_2 photoelectrodes at 1.23 V vs. RHE under constant illumination (100 mW cm^{-2}).

ciency for OER was estimated by coupling a gas chromatograph to the photoelectrochemical cell, highlighting the excellent selectivity of the developed systems towards oxygen evolution. After electrochemical testing (3 runs), the photoelectrodes were scratched from the FTO and XRD analysis was performed. The results showed the preservation of the crystal structure in the photoelectrodes confirming their promising stability (Supplementary Material, Fig. S14).

4. Conclusions

A dual strategy has been presented to overcome both the extensive carrier recombination and the intrinsically poor catalytic activity of MOFs for efficient OER. The two MOFs (MNH and UNH) with a suitable bandgap were selected to receive visible radiation from the sunlight, and were then interfaced with mesoporous TiO_2 to reduce bulk charge recombination. To improve the catalytic activity, CoPi as an earth abundance and low-cost water oxidation co-catalyst was deposited on the MOF surface. Functional characterization through linear sweep photovoltammetry, transient and steady-state chronoamperometric measurements and faradaic efficiency of photocatalysts proved that CoPi/MOFs/TiO_2 photoelectrodes possess notably boosted performance: photocurrent densities of 1.3 and 1.8 mA/cm^2 at 1.23 V vs. RHE in artificial seawater for CoPi/UNH/TiO_2 and CoPi /MNH/TiO_2, respectively, and display fast and reusable photocurrent. These photocurrent densities were nearly 26-fold higher compared to pristine MOFs with 0.07 mA·cm^{-2} for MNH and 0.05 mA·cm^{-2} for UNH. This is attributed to the presence of TiO_2 and CoPi co-catalyst, which enhanced the charge-separation and charge-injection efficiency towards OER, respectively. The PL intensities are consistent with the longer lifetime of photogenerated charge carriers in CoPi/MOF/TiO_2 composites. Our results showed that, MNH possesses higher OER activity compared to UNH probably due to the higher specific surface area of MNH. Finally, a remarkable Faradaic efficiency of > 93 % was estimated for OER, highlighting the excellent selectivity of the developed systems towards oxygen evolution. These findings offer a promising perspective to expand the photoelectrochemical applicability of MOFs to more complex electrochemical transformations.

5. Associated content

5.1. Supplementary Material

Cross-section view of two photocatalyst, X-ray photoelectron spectroscopy (XPS) analysis and Elemental ratios from XPS, Transient photoelectrochemical measurements of MOFs composite and results of energy-dispersive X-ray spectroscopy were detailed in SI. The UV-vis absorption spectra, Tauc plots and the maximum theoretical photocurrent, calculated charge-injection efficiencies of photoelectrodes (j-V curves of the samples in the presence of a hole scavenger (0.5M Na_2SO_3)) and charge-separation efficiencies of photoelectrodes are given in Fig S5-9 respectively.

6. Author's role

Niloufar Afzali: Investigation, Methodology, Data Curation, Writing- Original draft preparation

Reza Keshavarzi: Conceptualization, Methodology, Writing- Original draft preparation, Writing- Reviewing and Editing

Shahram Tangestaninejad: Conceptualization, Investigation, Supervision.

Sixto Gimenez: Conceptualization, Writing- Original draft preparation, Supervision, Writing- Reviewing and Editing

Valiollah Mirkhani: Investigation, Methodology, Visualization
Majid Moghadam: Investigation, Methodology
Iraj Mohammadpoor-Baltork: Investigation, Data Curation

Declaration of competing interest

The authors declare that they have no known competing financial interests or personal relationships that could have appeared to influence the work reported in this paper.

Acknowledgements

We acknowledge with appreciation the financial support from the University of Isfahan and Ministry of Science, Research and Technology Center for International Scientific Studies and Collaboration (CISSC). SG acknowledges the financial support from the Ministerio de Ciencia, Innovación y Universidades of Spain through funded project ENE2017-85087-C3-1-R.

Supplementary materials

Supplementary material associated with this article can be found, in the online version, at doi:10.1016/j.apmt.2021.101159.

References

[1] Z. Li, W. Luo, M. Zhang, J. Feng, Z. Zou, Photoelectrochemical cells for solar hydrogen production: current state of promising photoelectrodes, methods to improve their properties, and outlook, Energy Environ. Sci. 6 (2013) 347–370.
[2] M.G. Walter, E.L. Warren, J.R. McKone, S.W. Boettcher, Q. Mi, E.A. Santori, N.S. Lewis, Solar water splitting cells, Chem. Rev. 110 (2010) 6446–6473.
[3] K. Meyer, M. Ranocchiari, J.A. van Bokhoven, Metal organic frameworks for photo-catalytic water splitting, Energy Environ. Sci. 8 (2015) 1923–1937.
[4] K. Young, L. a. Martini, RL Milot, RC Snoeberger, VS Batista, C. a. Schmuttenmaer, RH Crabtree, GW Brudvig, Coord. Chem. Rev 256 (2012) 2503–2520.
[5] M.D. Karkas, O. Verho, E.V. Johnston, B.r. Åkermark, Artificial photosynthesis: molecular systems for catalytic water oxidation, Chem. Rev. 114 (2014) 11863–12001.
[6] A. Kudo, Y. Miseki, Heterogeneous photocatalyst materials for water splitting, Chem. Soc. Rev. 38 (2009) 253–278.
[7] T. Zhang, W. Lin, Metal–organic frameworks for artificial photosynthesis and photocatalysis, Chem. Soc. Rev. 43 (2014) 5982–5993.
[8] Y. An, B. Xu, Y. Liu, Z. Wang, P. Wang, Y. Dai, X. Qin, X. Zhang, B. Huang, Photocatalytic overall water splitting over MIL-125 (Ti) upon CoPi and Pt Co-catalyst deposition, ChemistryOpen 6 (2017) 701–705.
[9] K. Deng, Z. Hou, X. Li, C. Li, Y. Zhang, X. Deng, Z. Cheng, J. Lin, Aptamer-mediated up-conversion core/MOF shell nanocomposites for targeted drug delivery and cell imaging, Sci. Rep. 5 (2015) 7851.
[10] F. Soltanolkottabi, M.R. Talaie, S. Aghamiri, S. Tangestaninejad, Introducing a dual-step procedure comprising microwave and electrical heating stages for the morphology-controlled synthesis of chromium-benzene dicarboxylate, MIL-101 (Cr), applicable for CO2 adsorption, J. Environ. Manage. 250 (2019) 109416.
[11] J. Li, S. Cheng, Q. Zhao, P. Long, J. Dong, Synthesis and hydrogen-storage behavior of metal–organic framework MOF-5, Int. J. Hydrogen Energy 34 (2009) 1377–1382.
[12] N. Afzali, R. Kardanpour, F. Zadehahmadi, S. Tangestaninejad, M. Moghadam, V. Mirkhani, A. Mechler, I. Mohammadpoor-Baltork, M. Bahadori, Molybdenum (VI)-functionalized UiO-66 provides an efficient heterogeneous nanocatalyst in oxidation reactions, Appl. Organomet. Chem. 33 (2019) e5225.
[13] R.V. Jagadeesh, K. Murugesan, A.S. Alshammari, H. Neumann, M.-M. Pohl, J. Radnik, M. Beller, MOF-derived cobalt nanoparticles catalyze a general synthesis of amines, Science 358 (2017) 326–332.
[14] H. Zhao, Q. Xia, H. Xing, D. Chen, H. Wang, Construction of pillared-layer MOF as efficient visible-light photocatalysts for aqueous Cr (VI) reduction and dye degradation, ACS Sustain. Chem. Eng. 5 (2017) 4449–4456.
[15] D. Cardenas-Morcoso, R. Ifraemov, M. García-Tecedor, I. Liberman, S. Gimenez, I. Hod, A metal–organic framework converted catalyst that boosts photo-electrochemical water splitting, J. Mater. Chem. A 7 (2019) 11143–11149.
[16] W. Wang, X. Xu, W. Zhou, Z. Shao, Recent progress in metal-organic frameworks for applications in electrocatalytic and photocatalytic water splitting, Adv. Sci. 4 (2017) 1600371.
[17] K.T. Butler, C.H. Hendon, A. Walsh, Electronic chemical potentials of porous metal–organic frameworks, J. Am. Chem. Soc. 136 (2014) 2703–2706.
[18] D. Sun, Z. Li, Robust Ti-and Zr-based metal-organic frameworks for photocatalysis, Chin. J. Chem. 35 (2017) 135–147.
[19] H. Liu, J. Zhang, D. Ao, Construction of heterostructured ZnIn2S4@ NH2-MIL-125 (Ti) nanocomposites for visible-light-driven H2 production, Appl. Catal. B 221 (2018) 433–442.
[20] M. Amini, R. Keshavarzi, V. Mirkhani, M. Moghadam, S. Tangestaninejad, I. Mohammadpoor-Baltork, F. Sadegh, From dense blocking layers to different templated films in dye sensitized and perovskite solar cells: toward light transmittance management and efficiency enhancement, J. Mater. Chem. A 6 (2018) 2632–2642.
[21] F. Lin, D. Wang, Z. Jiang, Y. Ma, J. Li, R. Li, C. Li, Photocatalytic oxidation of thiophene on BiVO 4 with dual co-catalysts Pt and RuO 2 under visible light irradiation using molecular oxygen as oxidant, Energy Environ. Sci. 5 (2012) 6400–6406.
[22] R. Gonzalez-Huerta, G. Ramos-Sanchez, P. Balbuena, Oxygen evolution in Co–doped RuO2 and IrO2: experimental and theoretical insights to diminish electrolysis overpotential, J. Power Sources 268 (2014) 69–76.
[23] M. Hara, C.C. Waraksa, J.T. Lean, B.A. Lewis, T.E. Mallouk, Photocatalytic water oxidation in a buffered Tris (2, 2 '-bipyridyl) ruthenium complex-colloidal IrO2 system, J. Phys. Chem. A 104 (2000) 5275–5280.
[24] M.W. Kanan, D.G. Nocera, In situ formation of an oxygen-evolving catalyst in neutral water containing phosphate and Co2+, Science 321 (2008) 1072–1075.
[25] M. Barroso, A.J. Cowan, S.R. Pendlebury, M. Grätzel, D.R. Klug, J.R. Durrant, The role of cobalt phosphate in enhancing the photocatalytic activity of α-Fe2O3 toward water oxidation, J. Am. Chem. Soc. 133 (2011) 14868–14871.
[26] D.K. Zhong, D.R. Gamelin, Photoelectrochemical water oxidation by cobalt catalyst ("Co− Pi")/α-Fe2O3 composite photoanodes: oxygen evolution and resolution of a kinetic bottleneck, J. Am. Chem. Soc. 132 (2010) 4202–4207.
[27] D. Liu, L. Jing, P. Luan, J. Tang, H. Fu, Enhancement effects of cobalt phosphate modification on activity for photoelectrochemical water oxidation of TiO2 and mechanism insights, ACS Appl. Mater. Interfaces 5 (2013) 4046–4052.
[28] M. Bledowski, L. Wang, A. Ramakrishnan, O.V. Khavryuchenko, V.D. Khavryuchenko, P.C. Ricci, J. Strunk, T. Cremer, C. Kolbeck, R. Beranek, Visible-light photocurrent response of TiO 2–polyheptazine hybrids: evidence for interfacial charge-transfer absorption, PCCP 13 (2011) 21511–21519.
[29] S. Subudhi, G. Swain, S.P. Tripathy, K. Parida, UiO-66-NH2 Metal–organic frameworks with embedded MoS2 Nanoflakes for Visible-Light-Mediated H2 and O2 evolution, Inorg. Chem. 59 (2020) 9824–9837.
[30] A. Samal, S. Swain, B. Satpati, D.P. Das, B.K. Mishra, 3 D Co3 (PO4) 2–reduced graphene oxide flowers for photocatalytic water splitting: a Type II staggered heterojunction system, ChemSusChem 9 (2016) 3150–3160.
[31] J.H. Cavka, S. Jakobsen, U. Olsbye, N. Guillou, C. Lamberti, S. Bordiga, K.P. Lillerud, A new zirconium inorganic building brick forming metal organic frameworks with exceptional stability, J. Am. Chem. Soc. 130 (2008) 13850–13851.
[32] M. Dan-Hardi, C. Serre, T. Frot, L. Rozes, G. Maurin, C. Sanchez, G. Férey, A new photoactive crystalline highly porous Titanium(IV) Dicarboxylate, J. Am. Chem. Soc. 131 (2009) 10857–10859.
[33] N. Afzali, S. Tangestaninejad, R. Keshavarzi, V. Mirkhani, J. Nematollahi, M. Moghadam, I. Mohammadpoor-Baltork, M. Reimer, S. Olthof, A. Klein, Hierarchical Ti-Based MOF with Embedded RuO2 nanoparticles: a highly efficient photoelectrode for visible light water oxidation, ACS Sustain. Chem. Eng. (2020).
[34] J. Theerthagiri, K. Thiagarajan, B. Senthilkumar, Z. Khan, R.A. Senthil, P. Arunachalam, J. Madhavan, M. Ashokkumar, Synthesis of hierarchical cobalt phosphate nanoflakes and their enhanced electrochemical performances for supercapacitor applications, ChemistrySelect 2 (2017) 201–210.
[35] H. Song, Z. Sun, Y. Xu, Y. Han, J. Xu, J. Wu, T. Sun, H. Meng, X. Zhang, Fabrication of NH2-MIL-125 (Ti) incorporated TiO2 nanotube arrays composite anodes for highly efficient PEC water splitting, Sep. Purif. Technol. 228 (2019) 115764.
[36] F. Hegner, I. Herraiz-Cardona, D. Cardenas-Morcoso, N.r. López, J.-R.n. Galán–Mascarós, S. Gimenez, ACS Appl. Mater. Interfaces 9 (2017) 37671–37681.
[37] Z. Li, J.-D. Xiao, H.-L. Jiang, Encapsulating a Co (II) molecular photocatalyst in metal–organic framework for visible-light-driven H2 production: boosting catalytic efficiency via spatial charge separation, ACS Catal. 6 (2016) 5359–5365.
[38] X. Feng, J. Zhang, L. Yin, Enhanced cycling stability of Co3 (PO4) 2-coated LiMn2O4 cathode materials for lithium ion batteries, Powder Technol. 287 (2016) 77–81.
[39] R. Keshavarzi, V. Mirkhani, M. Moghadam, S. Tangestaninejad, I. Mohammadpoor-Baltork, Highly efficient dye sensitized solar cells based on ordered and disordered mesoporous titania thick templated films, J. Mater. Chem. A 3 (2015) 2294–2304.
[40] I. Ahmed, S.H. Jhung, Composites of metal–organic frameworks: preparation and application in adsorption, Mater. Today 17 (2014) 136–146.
[41] G. Wang, C.-T. He, R. Huang, J. Mao, D. Wang, Y. Li, Photoinduction of cu single atoms decorated on uio-66-nh2 for enhanced photocatalytic reduction of CO2 to liquid fuels, J. Am. Chem. Soc. 142 (2020) 19339–19345.
[42] S. Hu, M. Liu, K. Li, Y. Zuo, A. Zhang, C. Song, G. Zhang, X. Guo, Solvothermal synthesis of NH 2-MIL-125 (Ti) from circular plate to octahedron, CrystEngComm 16 (2014) 9645–9650.
[43] B. Zhang, J. Zhang, X. Tan, D. Shao, J. Shi, L. Zheng, J. Zhang, G. Yang, B. Han, MIL-125-NH2@ TiO2 core–shell particles produced by a post-solvothermal route for high-performance photocatalytic H2 production, ACS Appl. Mater. Interfaces 10 (2018) 16418–16423.
[44] X. Yin, H. Li, R. Yuan, J. Lu, Hierarchical self-supporting sugar gourd-shape MOF-derived NiCo2O4 hollow nanocages@ SiC nanowires for high-performance flexible hybrid supercapacitors, J. Colloid Interface Sci. 586 (2021) 219–232.
[45] W. Lv, Z. Liu, J. Lan, Z. Liu, W. Mi, J. Lei, L. Wang, Y. Liu, J. Zhang, Visible–light-induced reduction of hexavalent chromium utilizing cobalt phosphate

(Co-Pi) sensitized inverse opal TiO 2 as a photocatalyst, Catal. Sci. Technol. 7 (2017) 5687–5693.
[46] M. Wang, L. Yang, J. Yuan, L. He, Y. Song, H. Zhang, Z. Zhang, S. Fang, Heterostructured Bi 2 S 3@ NH 2-MIL-125 (Ti) nanocomposite as a bifunctional photocatalyst for Cr (vi) reduction and rhodamine B degradation under visible light, RSC Adv. 8 (2018) 12459–12470.
[47] L. Shen, W. Wu, R. Liang, R. Lin, L. Wu, Highly dispersed palladium nanoparticles anchored on UiO-66 (NH 2) metal-organic framework as a reusable and dual functional visible-light-driven photocatalyst, Nanoscale 5 (2013) 9374–9382.
[48] P. Barone, F. Stranges, M. Barberio, D. Renzelli, A. Bonanno, F. Xu, Study of band gap of silver nanoparticles—Titanium dioxide nanocomposites, J. Chem. 2014 (2014).
[49] S. Zhao, C. Li, H. Huang, Y. Liu, Z. Kang, Carbon nanodots modified cobalt phosphate as efficient electrocatalyst for water oxidation, J. Materiomics 1 (2015) 236–244.
[50] H.W. Jeong, T.H. Jeon, J.S. Jang, W. Choi, H. Park, Strategic modification of BiVO4 for improving photoelectrochemical water oxidation performance, J. Phys. Chem. C 117 (2013) 9104–9112.
[51] B. Klahr, S. Gimenez, F. Fabregat-Santiago, J. Bisquert, T.W. Hamann, Photoelectrochemical and impedance spectroscopic investigation of water oxidation with “Co–Pi”-coated hematite electrodes, J. Am. Chem. Soc. 134 (2012) 16693–16700.